Elastic and plastic mechanical properties of nanoparticle-based silica aerogels and xerogels

Michal Marszewski [a],[1], Ali Dashti [a], Patricia E. McNeil [b], Maggie Fox [b], Vivian Wall [c], Danielle M. Butts [b], Sophia C. King [c], Glareh N. Kashanchi [c], Sarah H. Tolbert [b],[c],[d], Bruce Dunn [b],[d], Laurent Pilon [a],[d],[e],[*]

[a] *Mechanical and Aerospace Engineering Department, University of California, Los Angeles, Los Angeles, CA, 90095, USA*
[b] *Department of Materials Science and Engineering, University of California, Los Angeles, Los Angeles, CA, 90095, USA*
[c] *Department of Chemistry and Biochemistry, University of California, Los Angeles, Los Angeles, CA, 90095, USA*
[d] *California NanoSystems Institute, University of California, Los Angeles, Los Angeles, CA, 90095, USA*
[e] *Institute of the Environment and Sustainability, University of California, Los Angeles, Los Angeles, CA, 90095, USA*

ARTICLE INFO

ABSTRACT

This paper reports and analyzes, for the first time, the effective Young's modulus and hardness of nanoparticle-based silica aerogels and xerogels with porosity ranging from 46 to 81%. Pure silica aerogel and xerogel monoliths were synthesized by (i) gelation of aqueous suspensions of silica nanoparticles on omniphobic substrates (PTFE or perfluorocarbon liquids), (ii) aging, (iii) drying at ambient temperature and pressure, and (iv) calcination. The aging and calcination conditions were varied to elucidate their effect on the mechanical properties of the monoliths. Both the effective Young's modulus and the hardness of the mesoporous slabs were measured by nanoindentation and were found to obey a power law as a function of the effective density. No effect of the synthetic conditions or structural parameters other than porosity were observed. Interestingly, the effective hardness was linearly proportional to the effective Young's modulus. The elastic properties of the present nanoparticle-based materials were compared with those of the molecular precursor-based silica aerogels and xerogels reported in the literature. A single relationship was proposed that can be used to estimate the effective Young's modulus of nanoparticle-based and molecular precursor-based silica aerogels and xerogels with porosity between 0 and 98% and Young's modulus between $\sim 10^{-4}$ and 70 GPa. Deposition of an alumina coating was also demonstrated as a way to increase the hardness of these mesoporous monoliths by a factor 2–13 for porosity of 40–73%. The experimental results and the accompanying analysis broaden the understanding of structure-property relationships in mesoporous silica and will help in the design and fabrication of mesoporous silica components.

Silica aerogels and xerogels are mesoporous materials with large specific surface areas (up to 1600 m^2 g^{-1}) [1], large porosities (up to 99.8%) [1], tunable pore sizes (2–150 nm) [1], low effective thermal conductivities (as low as 0.017 W m^{-1} K^{-1} in air at 300 K) [1], low effective refractive indices (as low as 1.007) [1], low effective dielectric constants (below 2.0) [1], low acoustic impedances (10^4–10^5 kg m^{-2} s^{-1}) [1], and high transparency [1]. Thanks to these exceptional properties, silica aerogels and xerogels are important functional materials used, for example, as thermal insulation for buildings and for cooling and heating systems [1], as optically transparent thermal insulation for

window applications [2–4] and for solar-thermal energy conversion systems [5–9], as optical supports with ultralow refractive index [10], as dielectric materials for microelectronics [11], as acoustic-impedance matching layers for piezoceramics [12], and as transparent dye hosts in laser amplification [13].

Silica aerogels and xerogels must often be machined to specific shape and size to make components for specific applications [14–18]. The usability of silica aerogels and xerogels as materials for a specific component and the associated machining processes are determined by their mechanical properties. The latter are often quantified using

---

Young's modulus E and hardness H to describe the material's responses to elastic and plastic deformations, respectively. Porous silica aerogels and xerogels are characterized by their *effective* Young's modulus E_{eff} and hardness H_{eff} which depend on porosity [19–26], just like their effective thermal conductivity k_{eff} [27], refractive index n_{eff} [28], and dielectric constant ε_{eff} [29]. In fact, E_{eff} has been shown to follow a power law expressed as [19–23]

$$E_{\text{eff}} = A\rho_{\text{eff}}^B, \tag{1}$$

where A and B are empirical constants ($B = 2.5$–3.8 for silica aerogels and xerogels [30]), $\rho_{\text{eff}} \approx (1 - \phi)\rho_{\text{SiO}_2}$ is the effective density of the porous silica with porosity ϕ while ρ_{SiO_2} is the density of bulk amorphous silica ($\rho_{\text{SiO}_2} \approx 2.2$ g cm^{-3}) [31]. In addition to porosity, E_{eff} has been shown to depend also on the synthesis and processing conditions [19, 21]. For example, Lemay et al. [19] showed that silica aerogels synthesized from tetramethoxysilane (TMOS) in acidic conditions had an effective Young's modulus one order of magnitude larger than those synthesized in basic conditions for the same porosity and with all other synthesis conditions remaining the same. Woignier et al. [21] observed the effective Young's modulus E_{eff} of supercritically-dried silica aerogels doubled when the synthesis conditions were changed from basic to either acidic or neutral while the porosity remained unchanged. The authors also observed a doubling in E_{eff} after the as-synthesized aerogels were calcined at 500 °C without significant changes in porosity. The authors attributed these changes in the elastic properties to changes in the connectivity of the building blocks of the porous materials, i.e., silica clusters or nanoparticles. In acidic conditions, molecular precursors hydrolyze and condense forming an entangled chain-like network similar to polymers [21]. By contrast, in basic conditions, silica precursors hydrolyze and condense forming very small silica nanoparticles (1–2 nm) that subsequently aggregate and fuse together by Ostwald ripening and covalent bonding [21]. Accordingly, the morphology formed under acidic conditions is more connected, resulting in stiffer material and larger effective Young's modulus [21]. Similarly, the larger Young's modulus E_{eff} of calcined aerogels was explained by the creation of new Si–O–Si bonds during the heat treatment, thus increasing the connectivity of the network [21].

Note that these and similar studies all focused on understanding only the elastic properties of mesoporous silica. However, few publications reported on the plastic properties of silica aerogels and xerogels [23–26]. In addition, most studies focused on silica materials synthesized from molecular precursors, such as TMOS. To the best of our knowledge, no study has investigated the mechanical properties of silica aerogels and xerogels synthesized from colloidal suspensions of silica nanoparticles. Ashkin et al. [22] observed that adding colloidal silica nanoparticles (Ludox HS-40, particle diameter = 15 nm) to the precursor solution lowered the effective Young's modulus of silica aerogels synthesized from potassium silicate. However, the study limited the amount of silica nanoparticles to only 25 wt% of the total mass of silica.

We recently reported two novel synthesis methods of ambiently dried, optically transparent, and thermally insulating silica aerogel [32] and xerogel [33] monoliths from colloidal suspensions of silica nanoparticles with porosity ϕ ranging from 46 to 81%. The present study reports, for the first time, the elastic and plastic mechanical properties of these nanoparticle-based mesoporous silica slabs. Their effective Young's modulus and hardness, measured by nanoindentation, were compared with data available in the literature for so-called molecular precursor-based silica aerogels and xerogels synthesized from precursors such as TMOS.

Details of the synthesis methods and of the structural, optical, and thermal characterization of the nanoparticle-based silica aerogels and xerogels are respectively provided in Refs. [32,33] and need not be repeated. Briefly, all aerogels and xerogels were synthesized from a commercial colloidal solution of silica nanoparticles [Nalco 2326, 15 wt % in water, NH$_3$ stabilized, measured particle diameter of 9 nm (Nalco

Chemical Company Naperville, IL, USA)] by sol-gel methods. The nanoparticle-based *xerogel* monoliths ($\phi = 46$–54%) were synthesized by concentrating the colloidal solution by evaporation until it gelled followed by drying the formed gels at or near ambient temperature and pressure [33]. The nanoparticle-based *aerogel* monoliths were synthesized by (1) adjusting the solution to pH = 5–8 with HCl to induce spontaneous gelation, (2) aging the formed gels at 25–80 °C for 1–21 days in a closed container, (3) exchanging the aqueous solution in the pores of the aged gels sequentially with ethanol, acetone, and finally octane, and (4) drying the exchanged gels in an octane-rich atmosphere at ambient temperature and pressure. In both sets of samples, some were synthesized on polytetrafluoroethylene (PTFE or Teflon) while others on perfluorocarbon (PFC) liquid [either perfluoropolyether oils Krytox GPL 100, GPL 104, and GPL 106 (Miller-Stephenson Chemical Company Inc., Danbury, CT, USA) or Fluorinert FC-70 or perfluoro(tetradecahydrophenanthrene) (PFTDHP) (SynQuest Laboratories, Inc. Alachua, FL, USA)]. In addition, some samples were calcined to remove any organic phase while others were analyzed as synthesized. Table 1 summarizes the synthesis conditions, structural characterization, and mechanical properties E_{eff} and H_{eff} of the nanoparticle-based silica aerogels and xerogels.

As a proof of concept, an alumina layer was deposited on nanoparticle-based silica xerogels and aerogels to increase their hardness. A Denton Desk II Deposition Sputterer (Denton Vacuum) was used to deposit the alumina layer where the deposition time and rate were calibrated to produce alumina coatings with approximate uniform thicknesses of 150–160 nm. Alongside the silica monoliths, an alumina layer was deposited on a mesoporous sol-gel–based silica thin film synthesized as described in Ref. [27] to characterize the alumina layer thickness via cross section scanning electron microscopy (SEM). SEM images were obtained using a field-emission scanning electron microscope (JEOL JSM-6700F) with 5 kV accelerating voltage and secondary electron detector configuration.

Depth profiles of the effective Young's modulus E_{eff} and hardness H_{eff} of the nanoparticle-based silica aerogels and xerogels were measured by the continuous stiffness measurement method using an MTS Nanoindenter XP instrument (MTS Nano Instruments Inc., Oak Ridge, TN, USA) equipped with a diamond Berkovich pyramidal tip. Each sample was indented at 16 different locations arranged in a 4 × 4 grid with 25 μm wide pitch using the strain rate of 0.05 sec^{-1}, harmonic displacement of 2 nm, frequency of 45 Hz, and maximum displacement of 2000 nm. Successful indentations (see Figure S1 in the SI for the example depth profiles) were used to calculate Young's modulus and hardness in the displacement range of 1000–1800 nm which were then averaged to yield the effective Young's modulus and hardness, as well as the associated standard deviation. The effective Poisson's ratio ν_{eff} of mesoporous silica was taken as $\nu_{\text{eff}} = 0.20$ based on the experimentally measured and numerically predicted values reported in Refs. [34,35].

Fig. 1 shows (a) the effective Young's modulus E_{eff} and (b) the effective hardness H_{eff} of nanoparticle-based mesoporous silica monoliths as functions of their effective density ρ_{eff}. The error bars correspond to two standard deviations or 95% confidence interval. Fig. 1 establishes that the effective density was the main factor affecting the elastic and plastic mechanical properties of the nanoparticle-based mesoporous silica monoliths. In fact, both the effective Young's modulus E_{eff} and hardness H_{eff} of all nanoparticle-based silica aerogels and xerogels increased by roughly 30 times when ρ_{eff} increased only by a factor 3 (Table 1). In addition, they both satisfied a power law relationship with respect to the effective density ρ_{eff} [Eq. (1)] given by

$$E_{\text{eff}} = 3.95\rho_{\text{eff}}^{3.34} \ \left(R^2 = 0.97\right) \ \text{and} \ H_{\text{eff}} = 0.35\rho_{\text{eff}}^{3.17} \ \left(R^2 = 0.95\right) \tag{2}$$

The power law dependence of E_{eff} vs. ρ_{eff} for molecular precursor-based silica aerogels and xerogels has been well documented [19–21] (if not well understood [30]) with a power law index in the range 2.5–3.8. By contrast, little has been elucidated about the relationship

Table 1
Synthesis conditions and structural and mechanical characterization of the ambiently-dried nanoparticle-based silica aerogels [32] and xerogels [33].

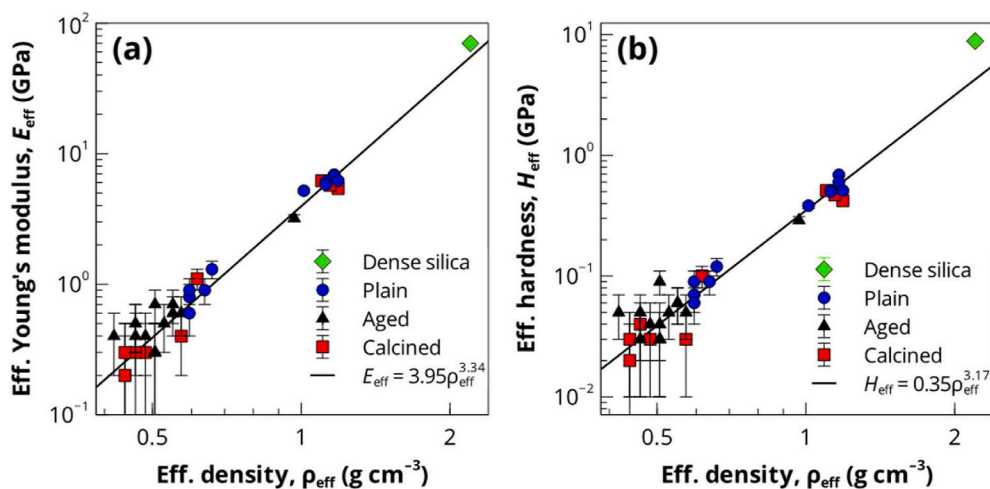| Sample	Substrate	Gelation	Aging temp./time	Drying solvent	Calcination	ρ_{eff} (g/cm³)	S_{BET} (m²/g)	ϕ	w_p (nm)	D_s	D_m	E_{eff} (GPa)	H_{eff} (GPa)
Fused silica	–	–	–	–	–	2.2	0	0	0	–	–	70.0	8.84
1[a]	PTFE	Evap.	25 °C/>3 days	Water	–	1.188	390	46	5.5	2.48	–	6.2	0.51
2[a]	PTFE	Evap.	25 °C/>3 days	Water	–	1.166	420	47	5.2	2.48	–	6.9	0.69
3	PTFE	Evap.	25 °C/>3 days	Water	–	1.166	420	47	5.2	2.48	–	6.8	0.60
4[a]	PTFE	Evap.	25 °C/>3 days	Water	–	1.122	430	49	5.2	2.48	–	6.1	0.51
5[a]	PTFE	Evap.	25 °C/>3 days	Water	–	1.122	430	49	5.2	2.48	–	5.8	0.50
6	PTFE	Evap.	30 °C/>3 days	Water	–	1.012	470	54	6.1	2.51	–	5.2	0.38
7[a]	PFC	Evap.	25 °C/>3 days	Water	450 °C/2 h	1.188	320	46	6.4	2.49	–	5.4	0.42
8[a]	PFC	Evap.	25 °C/>3 days	Water	450 °C/2 h	1.144	360	47	5.8	2.48	–	5.7	0.47
9	PFC	Evap.	25 °C/>3 days	Water	450 °C/2 h	1.100	360	49	5.8	2.51	–	6.2	0.51
10[b]	PTFE	pH	50 °C/1 day	Water	–	0.968	380	56	8.0	2.49	–	3.2	0.29
11[b]	PTFE	pH	25 °C/1 day	Octane	–	0.594	390	73	17.2	2.58	–	0.8	0.07
12[b]	PTFE	pH	25 °C/1 day	Octane	–	0.594	390	73	17.2	2.58	–	0.6	0.06
13[b]	PTFE	pH	25 °C/1 day	Octane	450 °C/4 h	0.616	390	72	18.3	2.59	1.33	1.1	0.10
14[b]	PTFE	pH	25 °C/1 day	Octane	–	0.638	360	71	16.8	2.58	1.15	0.9	0.09
15[b]	PTFE	pH	25 °C/1 day	Octane	–	0.594	390	73	17.6	2.62	1.23	0.9	0.09
16[b]	PTFE	pH	25 °C/21 days	Octane	–	0.660	400	70	13.5	2.55	1.14	1.3	0.12
17[b]	PTFE	pH	40 °C/3 days	Octane	450 °C/4 h	0.572	370	74	17.7	2.58	1.08	0.4	0.03
18[b]	PTFE	pH	50 °C/1 day	Octane	–	0.572	380	74	18.2	2.60	1.30	0.6	0.05
19[b]	PTFE	pH	50 °C/2 days	Octane	–	0.462	370	79	21.1	2.63	1.07	0.4	0.03
20[b]	PTFE	pH	50 °C/3 days	Octane	–	0.506	300	77	21.8	2.62	–	0.3	0.03
21[b]	PTFE	pH	50 °C/3 days	Octane	450 °C/4 h	0.484	370	78	22.6	2.62	–	0.3	0.03
22[b]	PFC (GPL)	pH	50 °C/4 days	Octane	450 °C/4 h	0.462	360	79	21.5	2.60	1.13	0.3	0.04
23[b]	PFC (FC-70)	pH	50 °C/4 days	Octane	–	0.506	350	77	19.4	2.62	1.05	0.7	0.09
24[b]	PFC (PFTDHP)	pH	50 °C/4 days	Octane	–	0.506	420	77	24.9	2.65	1.06	0.3	0.03
25[b]	PFC (PFTDHP)	pH	50 °C/4 days	Octane	–	0.506	420	77	24.9	2.65	1.06	0.3	0.04
26[b]	PFC (PFTDHP)	pH	50 °C/5 days	Octane	–	0.484	350	78	22.6	2.60	1.11	0.4	0.04
27[b]	PTFE	pH	50 °C/6 days	Octane	–	0.462	340	79	24.2	2.64	1.13	0.5	0.03
28[b]	PFC (GPL)	pH	50 °C/6 days	Octane	450 °C/4 h	0.440	340	80	26.0	2.64	1.27	0.3	0.03
29[b]	PFC (FC-70)	pH	50 °C/6 days	Octane	–	0.462	390	79	24.0	2.62	1.42	0.5	0.05
30[b]	PFC (PFTDHP)	pH	50 °C/6 days	Octane	–	0.506	350	77	25.9	2.64	1.23	0.3	0.03
31[b]	PFC (GPL)	pH	50 °C/7 days	Octane	450 °C/4 h	0.440	340	80	24.7	2.63	–	0.3	0.03
32[b]	PFC (FC-70)	pH	50 °C/14 days	Octane	450 °C/4 h	0.440	340	80	25.0	2.63	–	0.2	0.02
33[b]	PTFE	pH	60 °C/1 day	Octane	–	0.550	350	75	20.3	2.60	1.43	0.6	0.06
34[b]	PTFE	pH	60 °C/1 day	Octane	–	0.528	370	76	19.6	2.59	1.23	0.5	0.05
35[b]	PTFE	pH	60 °C/1 day	Octane	–	0.550	360	75	19.0	2.58	1.15	0.7	0.06
36[b]	PTFE	pH	80 °C/1 day	Octane	–	0.418	360	81	26.0	2.62	1.05	0.4	0.05

Notation.

[a] Synthesis details and structural and mechanical characterization adapted from Ref. [33].

[b] Synthesis details and structural characterization adapted from Ref. [32].

Fig. 1. (a) Effective Young's modulus E_{eff} and (b) effective hardness H_{eff} of the nanoparticle-based mesoporous silica monoliths as a function of their effective density ρ_{eff}. (i) *Dense silica* refers to the dense (non-porous) fused silica sample; (ii) *Plain* refers to all samples that were synthesized at 25–30 °C and not calcined; (iii) *Aged* refers to all samples that were aged at 50–80 °C and not calcined; and (iv) *Calcined* refers to all samples that were calcined. Note that all axes are in logarithmic scale. The error bars correspond to two standard deviations or 95% confidence interval. The solid black lines represent power law fits over all nanoparticle-based silica aerogels and xerogels given by Eq. (2).

between H_{eff} and ρ_{eff} [23–26].

Fig. 1 also indicates that the aging temperature (25–80 °C) and duration (1–21 days) and/or calcination (450 °C for either 2 or 4 h) had no direct effect on the trends of E_{eff} vs. ρ_{eff} and of H_{eff} vs. ρ_{eff} as almost all measurements fell within the experimental uncertainty from the power law predictions [Eq. (2)]. These processes strengthen the silica framework of molecular precursor-based mesoporous silica by (i) converting the unreacted molecular precursor remaining in the pore liquid after gelation into silica, (ii) converting partially hydrolyzed (Si–OR) and partially condensed (Si–OH) framework into silica, (iii) redistributing silica by Ostwald ripening (only aging), and (iv) densifying the silica framework (only calcination) [36]. As such, the lack of a correlation between aging conditions on E_{eff} vs.ρ_{eff} and of H_{eff} vs. ρ_{eff} is in contrast with the established knowledge that aging and calcination increase the strength of molecular precursor-based silica aerogels and xerogels [21, 36,37]. Interestingly, the actual effect of aging on the mechanical properties of molecular precursor-based mesoporous silica is unclear due to contradicting reported observations [25,38–40]. Specifically, aging has been reported to increase the effective shear modulus G_{eff} of wet molecular precursor-based silica gels expressed as $G_{eff} = E_{eff}[2(1 + \nu_{eff})]^{-1}$ [38,39]. However, measurements of the effective Young's modulus of dry molecular precursor-based silica aerogels showed no effect of aging [25,40].

In contrast to molecular precursor-based mesoporous silica, the present nanoparticle-based silica aerogels and xerogels were formed by aggregation of pre-formed dense silica nanoparticles. As a result, no precursor was present in the pore liquid and the framework can be assumed to be fully condensed after gelation. Thus, aging and calcination could not strengthen the silica framework the same way they strengthen molecular precursor-based mesoporous silica. In fact, since the aged materials had larger porosities, their effective Young's modulus and hardness were lower than those of the as-synthesized (or *plain*) samples.

Moreover, we employed residual analysis to elucidate whether specific surface area S_{BET}, peak pore width w_p, surface fractal dimension D_s, and/or mass fractal dimension D_m influenced the elastic and plastic mechanical properties of the nanoparticle-based mesoporous silica monoliths, in addition to their porosity (Figures S2 and S3 in the SI). The results show no secondary correlation with any of these structural parameters. Indeed, the residuals, defined as the relative differences between the experimental measurements and the predictions of Eq. (2) for both E_{eff} and H_{eff}, were randomly distributed around the mean. These observations indicate that mechanical properties of nanoparticle-based mesoporous silica monoliths depend only on their porosity.

Fig. 2 plots the effective hardness H_{eff} as a function of the effective Young's modulus E_{eff} for the synthesized nanoparticle-based silica aerogels and xerogels. It shows that despite the slightly different exponents in Eq. (2) (3.34 vs. 3.17) H_{eff} is almost linearly proportional to E_{eff} and can be approximated as

$$H_{eff} = 0.086 E_{eff} \qquad (3)$$

with a coefficient of determination $R^2 = 0.99$. Such correlation is interesting considering that Young's modulus and hardness describe a material's mechanical response in the very different elastic and plastic regimes. Similar correlations between H_{eff} and E_{eff} for mineralized tissue such as bone and tooth tissue, and for ceramic materials in general, were discussed by Oyen in Ref. [41]. The Young's modulus is typically estimated based on the unloading data, i.e., when the material's response is purely elastic [41]. However, hardness was originally proposed as a mechanical property to quantify plastic deformation in metals and is typically estimated at the peak load [41]. As plastic materials, metals exhibit almost purely plastic deformation during loading so that hardness calculated at the peak load truly quantifies their plastic properties [41]. However, ceramic and other brittle materials exhibit elastoplastic deformation during loading such that the material's response during
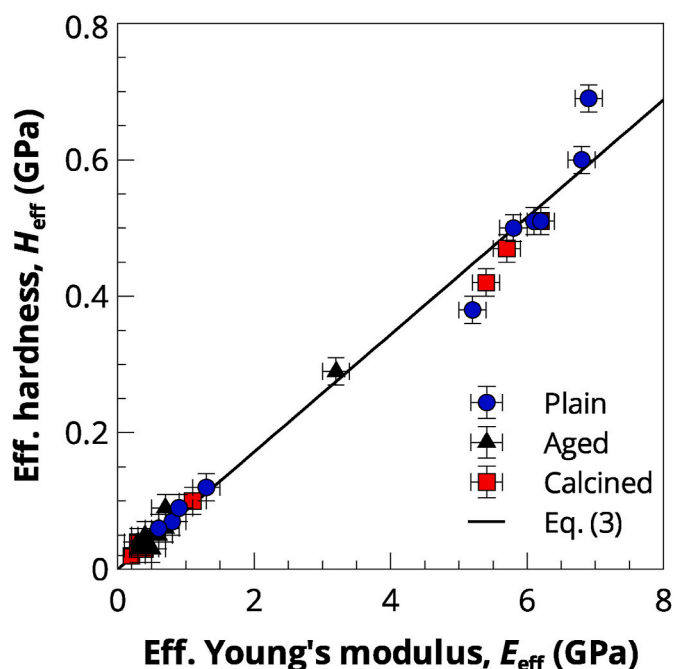

Fig. 2. Effective hardness H_{eff} as a function of effective Young's modulus E_{eff} for the nanoparticle-based mesoporous silica monoliths. (i) *Plain* refers to all samples that were synthesized at 25–30 °C and not calcined; (ii) *Aged* refers to all samples that were aged at 50–80 °C and not calcined; and (iii) *Calcined* refers to all samples that were calcined (see Table 1). The error bars correspond to two standard deviations or 95% confidence interval. The solid black line represents the linear fit given by Eq. (3).

mechanical loading is both elastic and plastic [41]. Thus, the hardness of brittle materials, including mesoporous silica, is affected by the contributions of both plastic and elastic behavior. This mixed response contributes to the observed correlation between H_{eff} and E_{eff}.

Finally, in order to reconcile Eqs. (2) and (3), the data for H_{eff} and E_{eff} as functions of ρ_{eff} were refitted by imposing the same power law index and the ratio of the pre-exponential factors to be 0.086 [Eq. (3)] to yield

$$E_{eff} = 3.99\rho_{eff}^{3.25} \quad \text{and} \quad H_{eff} = 0.34\rho_{eff}^{3.25}. \qquad (4)$$

without significantly changing the plots or affecting R^2, which remained 0.97 and 0.95 for E_{eff} and H_{eff}, respectively.

Fig. 3 compares the effective (a) Young's modulus E_{eff} and (b) hardness H_{eff} for the synthesized nanoparticle-based mesoporous silica monoliths (full symbols) with those reported in the literature for the precursor-based silica aerogels and xerogels (hollow symbols) synthesized under different conditions [19–26]. It indicates that for all aerogel and xerogel samples considered, the effective Young's modulus and hardness increased sharply with increasing effective density. In other words, porosity had a dominant effect on E_{eff} and H_{eff}. The power law index of individual sets of precursor-based mesoporous silica monoliths included in Fig. 3(a) ranged from 2.82 to 4.52 while the pre-exponential factor varied between approximately 0.5 and 28 GPa depending on the synthesis conditions. Despite these seemingly large differences in both factors, the literature results follow a very similar trend to that found for the present aerogels and xerogels [Eq. (2)] across a very wide range of effective densities varying from 0.05 to 2.2 g cm^{-3}.

Moreover, Fig. 3(b) illustrates the aforementioned limited availability of hardness data for silica aerogels and xerogels. This prevented a detailed comparison similar to that performed for the effective Young's modulus [Fig. 3(a)]. Still, the data compiled in Fig. 3(b) indicate that the effective hardness of the molecular precursor-based mesoporous silica also follows a power law with respect to the effective density ρ_{eff}, similar to that developed for nanoparticle-based aerogels and xerogels [Eq. (2)].
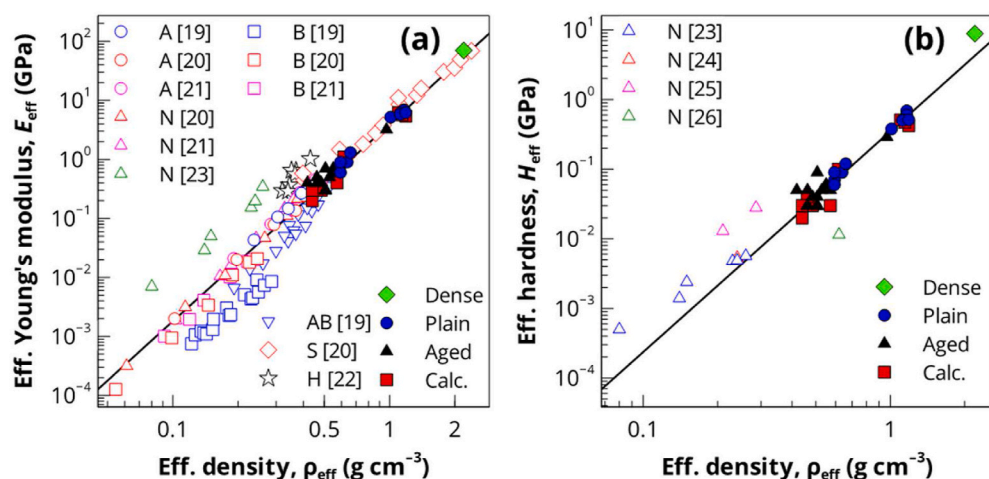
Fig. 3. Comparison of (a) effective Young's modulus E_{eff} and (b) effective hardness H_{eff} for the synthesized nanoparticle-based mesoporous silica monoliths (full symbols) with results reported in the literature for molecular precursor-based aerogels and xerogels (hollow symbols) [19–26]. (i) *A* and *B* refer to the as-synthesized molecular precursor-based one-step acid and base catalyzed aerogels, respectively; (ii) *N* refers to the as-synthesized molecular precursor-based aerogels synthesized in neutral pH conditions or in organic solvents; (iii) *AB* refers to the as-synthesized molecular precursor-based two-step acid-base catalyzed aerogels; (iv) *H* refers to the as-synthesized molecular precursor-based aerogels prepared with up to 25 wt% of colloidal silica nanoparticles; (v) *S* refers to the molecular precursor-based aerogels and xerogels densified by sintering above 1000 °C; (vi) *Dense* refers to the dense (non-porous) fused silica sample; (vii) *Plain* refers to the nanoparticle-based aerogels and xerogels that were synthesized at 25–30 °C and not calcined; (viii) *Aged* refers to the nanoparticle-based aerogels and xerogels that were aged at 50–80 °C and not calcined; and (ix) *Calc.* refers to the nanoparticle-based aerogels and xerogels that were calcined. Note that all axes are in logarithmic scale. The solid black lines represent the power law fits given by Eq. (2).
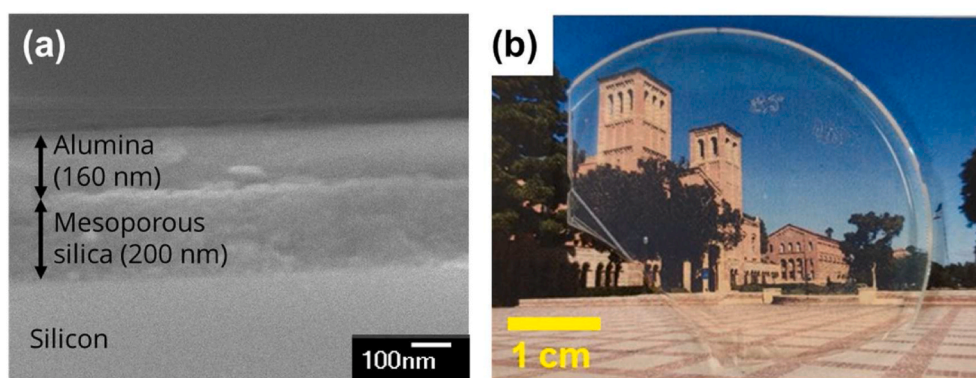

Fig. 4. (a) SEM image of a cross section of a mesoporous sol-gel silica thin film with deposited alumina hard coating. (b) Photograph of mesoporous nanoparticle-based monolith with alumina hard coating.

To increase the hardness of our mesoporous silica materials for practical applications, we successfully sputtered a dense, hard, and uniform alumina layer with thickness of approximately 160 nm on the mesoporous silica thin films without penetration into the pores, as illustrated in Fig. 4(a). Alumina hard coating was also deposited on mesoporous nanoparticle-based silica xerogel and aerogel monoliths using the same technique. The photograph in Fig. 4(b) shows that the uniform deposition of the alumina coating on a nanoporous silica xerogel did not affect the monolith's transparency and optical quality. Table 2 summarizes the effective hardness of the nanoparticle-based silica films and monoliths before and after deposition of alumina hard coatings. It indicates that depositing a 150–160 nm alumina hard coating increased the hardness of the mesoporous silica *films* by a factor 4 and increased the hardness of the nanoparticle-based slab *monoliths* with porosity 47% and 73% by factors of 2.3 and 13, respectively. The

effective hardness after alumina deposition varied from 0.8 GPa for the most porous monolith up to 3.7 GPa for the least porous thin film. As a reference, the hardness of polymethyl methacrylate (PMMA), a commercial variant of poly(methyl methacrylate) or acrylic used as a glass replacement in plastic windows, is 0.2–0.3 GPa [42].

In conclusion, the elastic and plastic mechanical properties of nanoparticle-based silica aerogels and xerogels measured by nanoindentation were reported and analyzed for the first time. The effective Young's modulus E_{eff} and hardness H_{eff} of the synthesized nanoparticle-based silica aerogels and xerogels, with porosity ranging from 46 to 81%, increased sharply with increasing effective density and obey a power law with respect to the effective density. No effects of the synthesis conditions or structural parameters other than porosity were observed. The effective hardness increased linearly with increasing effective Young's modulus, which was attributed to the elastoplastic

Table 2

Summary of characterization of a nanoparticle-based mesoporous silica thin films, nanoparticle-based silica xerogel and aerogel, before and after deposition of alumina hard coating.

Sample	Alumina thickness (nm)	Porosity (%)	Hardness before deposition (GPa)	Hardness after deposition (GPa)
Thin film	150–160	40	0.9	3.7
2	150–160	47	0.7	1.6
12	150–160	73	0.06	0.8

deformation of mesoporous silica during loading. Comparison of the mechanical properties of the nanoparticle-based mesoporous silica synthesized in this study with those of the precursor-based silica aerogels and xerogels reported in the literature indicated that they follow similar power law trends. This study broadened the understanding of the relationships between structure and elastic and plastic mechanical properties of mesoporous silica. The results can be used in the design and machining of mesoporous silica components.

CRediT authorship contribution statement

Michal Marszewski: Conceptualization, Methodology, Formal analysis, Data curation, Visualization, Writing – original draft. **Ali Dashti:** Investigation, Methodology, Formal analysis, Data curation, Visualization. **Patricia E. McNeil:** Resources, Investigation. **Maggie Fox:** Resources, Investigation. **Vivian Wall:** Resources, Investigation. **Danielle M. Butts:** Resources, Investigation. **Sophia C. King:** Resources, Investigation. **Glareh N. Kashanchi:** Resources, Investigation. **Sarah H. Tolbert:** Methodology, Supervision, Funding acquisition. **Bruce Dunn:** Methodology, Supervision, Funding acquisition. **Laurent Pilon:** Conceptualization, Methodology, Project administration, Supervision, Writing – review & editing, Funding acquisition.

Declaration of competing interest

The authors declare that they have no known competing financial interests or personal relationships that could have appeared to influence the work reported in this paper.

Acknowledgement

Appendix A. Supplementary data

Supplementary data to this article can be found online at https://doi.org/10.1016/j.micromeso.2021.111569.

References

[1] N. Hüsing, U. Schubert, Aerogels—airy materials: Chemistry, structure, and properties, Angew. Chem. Int. Ed. 37 (1998) 22–45, https://doi.org/10.1002/(SICI)1521-3773(19980202)37:1/2<22::AID-ANIE22>3.0.CO;2-I.

[2] V. Wittwer, Development of aerogel windows, J. Non-Cryst. Solids 145 (1992) 233–236, https://doi.org/10.1016/S0022-3093(05)80462-4.

[3] K.I. Jensen, J.M. Schultz, F.H. Kristiansen, Development of windows based on highly insulating aerogel glazings, J. Non-Cryst. Solids 350 (2004) 351–357, https://doi.org/10.1016/j.jnoncrysol.2004.06.047.

[4] Q. Zhu, Y. Li, Z. Qiu, Research progress on aerogels as transparent insulation materials, in: K. Cen, Y. Chi, F. Wang (Eds.), Chall. Power Eng. Environ, Springer, Berlin, Heidelberg, 2007, pp. 1117–1121, https://doi.org/10.1007/978-3-540-76694-0_207.

[5] A. Nordgaard, W. Beckman, Modeling of flat-plate collectors based on monolithic silica aerogel, Sol. Energy 49 (1992) 387–402, https://doi.org/10.1016/0038-092X(92)90111-M.

[6] L.A. Weinstein, J. Loomis, B. Bhatia, D.M. Bierman, E.N. Wang, G. Chen, Concentrating solar power, Chem. Rev. 115 (2015) 12797–12838, https://doi.org/10.1021/acs.chemrev.5b00397.

[7] K. McEnaney, L. Weinstein, D. Kraemer, H. Ghasemi, G. Chen, Aerogel-based solar thermal receivers, Nanomater. Energy 40 (2017) 180–186, https://doi.org/10.1016/j.nanoen.2017.08.006.

[8] E. Strobach, B. Bhatia, S. Yang, L. Zhao, E.N. Wang, High temperature annealing for structural optimization of silica aerogels in solar thermal applications, J. Non-Cryst. Solids 462 (2017) 72–77, https://doi.org/10.1016/j.jnoncrysol.2017.02.009.

[9] L. Zhao, B. Bhatia, S. Yang, E. Strobach, L.A. Weinstein, T.A. Cooper, G. Chen, E. N. Wang, Harnessing heat beyond 200 °C from unconcentrated sunlight with

[10] nonevacuated transparent aerogels, ACS Nano 13 (2019) 7508–7516, https://doi.org/10.1021/acsnano.9b02976.

[10] M. Schmidt, G. Boettger, M. Eich, W. Morgenroth, U. Huebner, R. Boucher, H. G. Meyer, D. Konjhodzic, H. Bretinger, F. Marlow, Ultralow refractive index substrates–a base for photonic crystal slab waveguides, Appl. Phys. Lett. 85 (2004) 16–18, https://doi.org/10.1063/1.1767962.

[11] A.C. Pierre, G.M. Pajonk, Chemistry of aerogels and their applications, Chem. Rev. 102 (2002) 4243–4266, https://doi.org/10.1021/cr0101306.

[12] J. Gross, J. Fricke, L.W. Hrubesh, Sound propagation in SiO2 aerogels, J. Acoust. Soc. Am. 91 (1992) 2004–2006, https://doi.org/10.1121/1.403684.

[13] S. Murai, K. Fujita, K. Nakanishi, K. Hirao, Fabrication of dye-infiltrated macroporous silica for laser amplification, J. Non-Cryst. Solids 345–346 (2004) 438–442, https://doi.org/10.1016/j.jnoncrysol.2004.08.059.

[14] I. Adachi, S. Fratina, T. Fukushima, A. Gorišek, T. Iijima, H. Kawai, M. Konishi, S. Korpar, Y. Kozakai, P. Križan, T. Matsumoto, Y. Mazuka, S. Nishida, S. Ogawa, S. Ohtake, R. Pestotnik, S. Saitoh, T. Seki, T. Sumiyoshi, M. Tabata, Y. Uchida, Y. Unno, S. Yamamoto, Study of highly transparent silica aerogel as a RICH radiator, Nucl. Instrum. Methods Phys. Res. Sect. Accel. Spectrometers Detect. Assoc. Equip. 553 (2005) 146–151, https://doi.org/10.1016/j.nima.2005.08.022.

[15] K.A.D. Obrey, R.D. Day, D. Hatch, B.F. Espinoza, S. Feng, B.M. Patterson, Manufacturing complex silica aerogel target components, Fusion Sci. Technol. 55 (2009) 490–498, https://doi.org/10.13182/FST55-4-490.

[16] L.W. Hrubesh, L.E. Keene, V.R. Latorre, Dielectric properties of aerogels, J. Mater. Res. 8 (1993) 1736–1741, https://doi.org/10.1557/JMR.1993.1736.

[17] K.A.D. Obrey, F. Fierro, J. Martinez, R. Randolph, D.W. Schmidt, Utilizing conventional machining tools with customized machining techniques to manufacture multifaceted targets, Fusion Sci. Technol. 63 (2013) 247–251, https://doi.org/10.13182/FST63-2-247.

[18] R.B. Randolph, J.A. Oertel, T. Cardenas, C.E. Hamilton, D.W. Schmidt, B. M. Patterson, F. Fierro, D. Capelli, Dry-machining of aerogel foams, CH foams, and specially engineered foams using turn-milling techniques, Fusion Sci. Technol. 73 (2018) 187–193, https://doi.org/10.1080/15361055.2017.1356196.

[19] J.D. Lemay, T.M. Tillotson, L.W. Hrubesh, R.W. Pekala, Microstructural dependence of aerogel mechanical properties, MRS Proc 180 (1990) 321, https://doi.org/10.1557/PROC-180-321.

[20] T. Woignier, J. Reynes, A. Hafidi Alaoui, I. Beurroies, J. Phalippou, Different kinds of structure in aerogels: relationships with the mechanical properties1Presented at the 7th International Conference on Non-Crystalline Materials, J. Non-Cryst. Solids 241 (1998) 45–52, https://doi.org/10.1016/S0022-3093(98)00747-9. Cagliari, Italy, 15–19 September 1997.1.

[21] T. Woignier, J. Phalippou, R. Vacher, Parameters affecting elastic properties of silica aerogels, J. Mater. Res. 4 (1989) 688–692, https://doi.org/10.1557/JMR.1989.0688.

[22] D. Ashkin, R.A. Haber, J.B. Wachtman, Elastic properties of porous silica derived from colloidal gels, J. Am. Ceram. Soc. 73 (1990) 3376–3381, https://doi.org/10.1111/j.1151-2916.1990.tb06464.x.

[23] M. Moner-Girona, E. Martínez, A. Roig, E. Esteve, E. Molins, Mechanical properties of silica aerogels measured by microindentation: influence of sol–gel processing parameters and carbon addition, J. Non-Cryst. Solids 285 (2001) 244–250, https://doi.org/10.1016/S0022-3093(01)00462-8.

[24] K.E. Parmenter, F. Milstein, Mechanical properties of silica aerogels, J. Non-Cryst. Solids 223 (1998) 179–189, https://doi.org/10.1016/S0022-3093(97)00430-4.

[25] E.M. Lucas, M.S. Doescher, D.M. Ebenstein, K.J. Wahl, D.R. Rolison, Silica aerogels with enhanced durability, 30-nm mean pore-size, and improved immersibility in liquids, J. Non-Cryst. Solids 350 (2004) 244–252, https://doi.org/10.1016/j.jnoncrysol.2004.07.074.

[26] R. Yokokawa, J.-A. Paik, B. Dunn, N. Kitazawa, H. Kotera, C.-J. Kim, Mechanical properties of aerogel-like thin films used for MEMS, J. Micromech. Microeng. 14 (2004) 681–686, https://doi.org/10.1088/0960-1317/14/5/004.

[27] Y. Yan, S.C. King, M. Li, T. Galy, M. Marszewski, J.S. Kang, L. Pilon, Y. Hu, S. H. Tolbert, Exploring the effect of porous structure on thermal conductivity in templated mesoporous silica films, J. Phys. Chem. C 123 (2019) 21721–21730, https://doi.org/10.1021/acs.jpcc.9b03767.

[28] T. Galy, M. Marszewski, S. King, Y. Yan, S.H. Tolbert, L. Pilon, Comparing methods for measuring thickness, refractive index, and porosity of mesoporous thin films, Microporous Mesoporous Mater. (2019) 109677, https://doi.org/10.1016/j.micromeso.2019.109677.

[29] C.M. Flannery, C. Murray, I. Streiter, S.E. Schulz, Characterization of thin-film aerogel porosity and stiffness with laser-generated surface acoustic waves, Thin Solid Films 388 (2001) 1–4, https://doi.org/10.1016/S0040-6090(01)00827-6.

[30] H.-S. Ma, A.P. Roberts, J.-H. Prévost, R. Jullien, G.W. Scherer, Mechanical structure–property relationship of aerogels, J. Non-Cryst. Solids 277 (2000) 127–141, https://doi.org/10.1016/S0022-3093(00)00288-X.

[31] J.R. Rumble (Ed.), CRC Handbook of Chemistry and Physics, 98th edition 2017-2018, CRC Press, Taylor & Francis Group, New York, 2017.

[32] M. Marszewski, S.C. King, T. Galy, G.N. Kashanchi, A. Dashti, Y. Yan, M. Li, D. M. Butts, P.E. McNeil, E. Lan, B. Dunn, S.H. Tolbert, L. Pilon, Transparent silica aerogel slabs synthesized from nanoparticle colloidal suspensions at near ambient conditions on omniphobic liquid substrates, J. Colloids Interface Sci. 606 (2022) 884–897, https://doi.org/10.1016/j.jcis.2021.07.159.

[33] M. Marszewski, S.C. King, Y. Yan, T. Galy, M. Li, A. Dashti, D.M. Butts, J.S. Kang, P. E. McNeil, E. Lan, B. Dunn, Y. Hu, S.H. Tolbert, L. Pilon, Thick transparent nanoparticle-based mesoporous silica monolithic slabs for thermally insulating window materials, ACS Appl. Nano Mater. 2 (2019) 4547–4555, https://doi.org/10.1021/acsanm.9b00903.

[34] J. Gross, G. Reichenauer, J. Fricke, Mechanical properties of SiO 2 aerogels, J. Phys. Appl. Phys. 21 (1988) 1447, https://doi.org/10.1088/0022-3727/21/9/020.

[35] S.P. Patil, A. Rege, Sagardas, M. Itskov, B. Markert, Mechanics of nanostructured porous silica aerogel resulting from molecular dynamics simulations, J. Phys. Chem. B 121 (2017) 5660–5668, https://doi.org/10.1021/acs.jpcb.7b03184.

[36] C.J. Brinker, G.W. Scherer, Sol-gel Science: the Physics and Chemistry of Sol-Gel Processing, Academic Press, Boston, 1990.

[37] H. Maleki, L. Durães, A. Portugal, An overview on silica aerogels synthesis and different mechanical reinforcing strategies, J. Non-Cryst. Solids 385 (2014) 55–74, https://doi.org/10.1016/j.jnoncrysol.2013.10.017.

[38] S. Hæreid, M. Dahle, S. Lima, M.-A. Einarsrud, Preparation and properties of monolithic silica xerogels from TEOS-based alcogels aged in silane solutions, J. Non-Cryst. Solids 186 (1995) 96–103, https://doi.org/10.1016/0022-3093(95)00039-9.

[39] R.A. Strøm, Y. Masmoudi, A. Rigacci, G. Petermann, L. Gullberg, B. Chevalier, M.-A. Einarsrud, Strengthening and aging of wet silica gels for up-scaling of aerogel preparation, J. Sol. Gel Sci. Technol. 41 (2007) 291–298, https://doi.org/10.1007/s10971-006-1505-7.

[40] H. Hdach, T. Woignier, J. Phalippou, G.W. Scherer, Effect of aging and pH on the modulus of aerogels, J. Non-Cryst. Solids 121 (1990) 202–205, https://doi.org/10.1016/0022-3093(90)90132-6.

[41] M.L. Oyen, Nanoindentation hardness of mineralized tissues, J. Biomech. 39 (2006) 2699–2702, https://doi.org/10.1016/j.jbiomech.2005.09.011.

[42] E. Amitay-Sadovsky, H.D. Wagner, Evaluation of Young's modulus of polymers from Knoop microindentation tests, Polymer 39 (1998) 2387–2390, https://doi.org/10.1016/S0032-3861(97)00550-8.